Chinese Chemical Letters 37 (2026) 112097

Contents lists available at ScienceDirect

Chinese Chemical Letters

journal homepage: www.elsevier.com/locate/cclet

Strain-gated tactile-to-pain sensing and vectorial mapping with recyclable e-skin

Xiaohui Yu[a,b], Guanpeng Zhou[a], Siyan Li[a], Yuanfeng Wang[a], Juan Zhang[a], Xiaotong Fan[b], Xiaoshan Fan[c], Jiajia Shen[a,*], Hui Ma[a,*], Zibiao Li[b,d,e,*]

[a] Center for Collaborative Innovation in Health-Fiber Electronics, College of Material and Textile Engineering, Jiaxing University, Jiaxing 314001, China
[b] Institute of Sustainability for Chemicals, Energy and Environment (ISCE2), Agency for Science, Technology and Research (A*STAR), Singapore 627833, Republic of Singapore
[c] School of Medicine, Huanghe Science and Technology University, Zhengzhou 450061, China
[d] Institute of Materials Research and Engineering (IMRE), Agency for Science, Technology and Research (A*STAR), Singapore 138634, Republic of Singapore
[e] Department of Materials Science and Engineering, National University of Singapore, Singapore 117576, Republic of Singapore

ARTICLE INFO

Article history:
Received 9 September 2025
Revised 7 November 2025
Accepted 10 November 2025
Available online 11 November 2025

Keywords:
Tactile-pain sensing
Flexible electronics
Eutectogel
e-skin
Recyclability

ABSTRACT

Realizing biologically authentic tactile–pain sensing in flexible electronic skins (e-skins) requires materials that combine linear touch encoding with strain-gated pain signaling, while also offering spatially resolved stimulus mapping and sustainable recyclability. Here, we present a recyclable neurothreshold-mimetic eutectogel (NeuroThres-Gel) based on a strain-induced percolation threshold modulation strategy. The prepared eutectogel demonstrated shear-thinning rheology, thermoplastic reprocessability, and environmental stability in wide temperature window. Under uniaxial strain, the conductive network remains intact and reversible up to a programmable critical strain (ε_t) of 80 %. Beyond this threshold, geometric percolation collapse occurs, resulting in a sharp, nonvolatile resistive transition that mimics neuronal action potential firing and enables strain-gated pain-like signaling. Direct-ink-writing (DIW) of NeuroThres-Gel yielded microstructured sensor arrays with volumetrically distributed receptive fields, achieving spatially resolved, vectorial pain mapping. Critically, after five melt-recycle cycles, the NeuroThres-Gel sensors retained excellent spatial nociceptive perception and stable mechanical strength, highlighting the closed-loop recyclability enabled by the dynamic cross-linked network. Collectively, NeuroThres-Gel integrated programmable tactile-to-pain conversion, directional nociceptive sensing, and sustainable recyclability into a single platform, charting a pathway toward next-generation adaptive prosthetic feedback systems and human–machine interfaces.

© 2026 Published by Elsevier B.V. on behalf of Chinese Chemical Society and Institute of Materia Medica, Chinese Academy of Medical Sciences.

Pain perception is a fundamental mechanism by which organisms avoid injury, primarily relying on the threshold response of peripheral nerve endings to external stimulis [1,2]. This biological intelligence is orchestrated through the dynamic switching of peripheral nerves and the coordinated excitation–inhibition balance within the dorsal horn of the spinal cord [3,4]. To emulate this sophisticated multimodal sensing in electronic skin (e-skin), devices must replicate both linear tactile encoding and discrete nociceptive switching [5]. Most flexible sensors today rely on continuous, linear resistance changes and lack true threshold behavior [6,7]. Current research endeavors to replicate this mechanism by engineering stepwise responses in the gauge factor (GF): under strains below a critical value (ε_t), piezoresistive network deforms reversibly, yielding a moderat GF value analogous to tactile sensing; when $\varepsilon > \varepsilon_t$, the conductive network undergoes a percolation phase transition, triggering a sharp increase of GF that mimics pain-like warning signals [8]. This nonvolatile resistive switch parallels neuronal action potentials in its threshold gating and high-gain output [4,9]. Nevertheless, two key challenges persist: (1) Precise tuning of GF is constrained by the stochastic spatial distribution and agglomeration of conductive fillers, which broadens the percolation threshold and reduces sensitivity control [10,11]; (2) Programmable adjustment of the nociceptive threshold ε_t requires engineered network architectures at the nanoscale to reliably shift the critical strain for percolation collapse. Addressing these challenges is essential for advancing truly biomimetic, integrated tactile–nociceptive e-skin platforms.

* Corresponding authors.
E-mail addresses: jjshen@zjxu.edu.cn (J. Shen), mahui@zjxu.edu.cn (H. Ma), lizb@imre.a-star.edu.sg (Z. Li).

https://doi.org/10.1016/j.cclet.2025.112097
1001-8417/© 2026 Published by Elsevier B.V. on behalf of Chinese Chemical Society and Institute of Materia Medica, Chinese Academy of Medical Sciences.

To further advance tactile–nociceptive integration, it is equally important to realize spatial vector decoding of noxious stimuli, akin to biological systems [12,13]. In living skin, this capability hinges on the three-dimensional (3D) topology of peripheral neural networks: free nerve endings at the epidermal–dermal junction branch into intricate 3D networks that pinpoint stimulus direction [14,15]. In the development of e-skin, truly 3D network constructs can establish volumetrically distributed "receptive fields" enabling the encoding of both pain depth and directional information [16–18]. Extrusion-based direct-ink-writing (DIW) has recently emerged as a robust fabrication method of choice for 3D e-skins due to its high design flexibility, low cost, and broad material compatibility [19–21]. Thermoplastic hydrogels, leveraging their excellent shear-thinning rheology and reversible dynamic cross-linking, have been widely adopted for DIW-based construction of 3D e-skin scaffolds [22,23]. However, their deployment is hampered by an intrinsic structure–function trade-off: dynamic-bond-based thermoplastic materials afford excellent reprocessability, yet the as-printed architectures often suffer from poor shape fidelity and mechanical performance [24–26]; conversely, the introduction of permanent covalent cross-links markedly improves printing stability, but irrevocably converts the material into a thermoset, drastically limiting its recyclability. Additionally, the high water content and inherent vapor permeability of conventional hydrogels compromise the environmental stability of printed sensor arrays [27,28]. Thus, realizing a single material platform that simultaneously delivers fully thermoplastic recyclability, high-fidelity 3D printability, enhanced environmental stablilty, and programmable GF modulation is the unmet demand for the development of next generation smart e-skins.

Herein, we presented a recyclable neurothreshold–mimetic eutectogel (NeuroThres–Gel) e-skin that harnessed strain–induced percolation threshold modulation to achieve biomimetic strain-programmable tactile–to–pain switching and vectorial pain mapping (Fig. 1). By ingeniously integrating dithiothreitol-functionalized Ag nanowires (D-Ag NWs) as dual-role conductive fillers and dynamic cross–linkers within deep eutectic solvents (DES)–plasticized poly(vinyl alcohol) (PVA) matrix, we constructed a robust yet recyclable network eutectogel that seamlessly merges sensitive mechanoresponsivity with full recyclability. Notably, the sensor's biomimetic pain logic arose from strain-triggered geometric percolation collapse: under small strains, the D-Ag NWs network undergoes topological rearrangement *via* reversible sliding/rotation (tactile mode), while surpassing a critical strain induces fractal dimension breakdown of the conductive pathways, driving an abrupt non-volatile resistive switching (pain mode) that emulates neuronal action potential thresholds. Meanwhile, the homogeneously dispersed D–Ag NWs could form dense yet reversible hydrogen–bond interactions with the PVA polymer chains, enhancing both mechanical strength and elasticity of the traget material. Furthermore, the thermally responsive dissociation–reassociation of dynamic bonds imparted NeuroThres-Gel with intriguing shear-thinning behavior, enabling direct compatibility with DIW-based fabrication of microstructured sensor arrays. In addition, the NeuroThres-Gel exhibited excellent thermoplasticity, recyclability, and environmental stability, overcoming the common pitfalls of hydrogel-based sensors. As a proof of concept, by patterning the thermoplastic NeuroThres–Gel into customizable microstructured arrays *via* DIW 3D printing method, each sensing element functions as an independent tactile–to–pain converter, enabling spatially resolved, multi–directional detection of noxious stimuli. This neuro-inspired design paradigm-synergizing strain-gated neuromorphic signaling, microarchitecture-driven vectorial sensing, and closed-loop material cyclability-establishes a transformative platform for adaptive prosthetic feedback systems and human-machine interfaces requiring biologically authentic somatosensory emulation.

Inspired by the hierarchical mechanoelectrical coupling behavior in biological somatosensory systems, particularly the interlocked collagen-nerve fiber networks that enable directional pain perception, we developed a neurothreshold-mimetic nanocomposite eutectogel comprising a DES plasticized PVA matrix which dynamically cross-linked by D-Ag NWs (Fig. 2A). The thiol groups of DTT are known to form robust Ag–S coordination bonds with the surface of Ag NWs, imparting dual functionality by simulta-

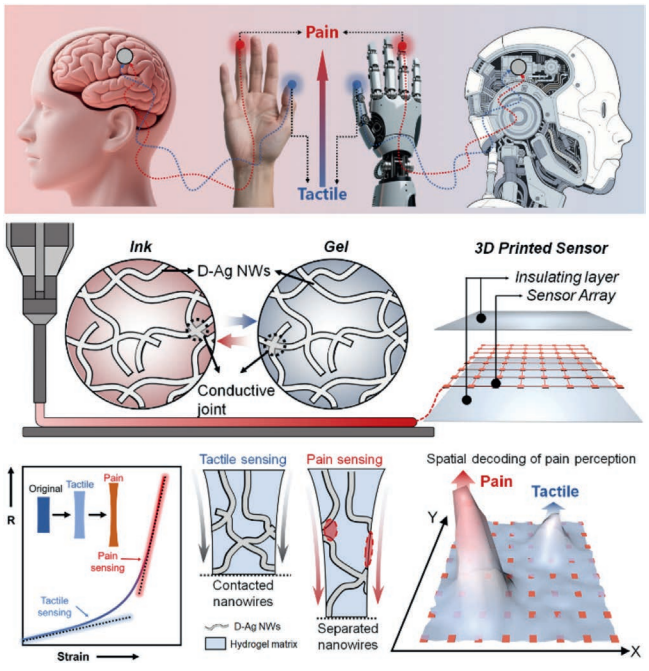


Fig. 1. Schematic of NeuroThres-Gel with D-Ag NWs integrated dynamic networks: Strain-induced percolation collapse enabled resistive switching for tactile-to-pain perception, while the thermally responsive dynamic cross-linked network allowed DIW microfabrication for bioinspired e-skin applications.

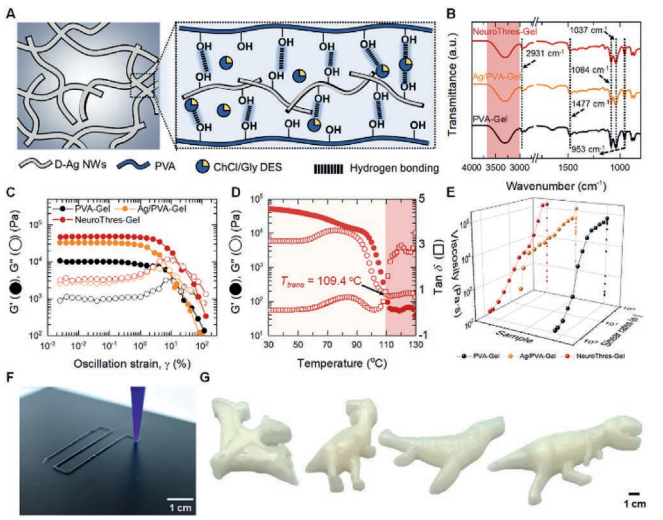


Fig. 2. Network structure of the eutectogels. (A) Schematic illustration of the network architecture and dynamic hydrogen bonding interactions within the NeuroThres–Gel. (B) FT-IR spectrum of the samples. (C) Amplitude oscillation strain sweeping modulus curves of different samples. (D) Temperature sweeping curves of NeuroThres-Gel. (E) Apparent viscosity of different inks as the function of shear rate at the temperature of 130 °C. Photographs of (F) the 3D printing process of the NeuroThres–Gel ink and (G) its remolded samples in different shapes.

neously providing highly conductive pathways and dynamic cross-linking sites [29,30]. Meanwhile, choline chloride-ethylene glycol (EG) DES (ChCl-EG DES) was employed as an alternative to conventional aqueous solvents for conductive hydrogels [27,31]. In this system, ChCl functioned as the hydrogen bond acceptor, while EG acts as the hydrogen bond donor. Concurrently, dense, yet dynamic, hydrogen-bonded domains between D-Ag NWs, PVA chains, and DES matrix ensured uniform filler dispersion and enhanced mechanical integrity [32–34]. Meanwhile, the strong hydrogen-bond interactions between ChCl and EG significantly lower the freezing point and volatility of the resulting DES, providing enhanced thermal and environmental stability of the prepared gels [35]. Moreover, the intrinsic electrostatic interactions between N^+ and Cl^- ions further improved the ionic conductivity of the DES as well as the composite eutectogel [36]. These characteristics collectively contributed to the high ionic conductivity and adjustable mechanical performance of the resulted eutectogel systems.

Fourier-transform infrared (FT-IR) spectroscopy was employed to elucidate the chemical structure and intermolecular interactions within the polymeric matrix. As shown in Fig. 2B, all the samples exhibited obvious peaks at 2931 and 1084 cm^{-1}, which corresponded to the C-H stretching vibration and C-O stretching of PVA presented in the composite gel matrix. Meanwhile, the characteristic peak at 953 cm^{-1} could be assigned to C-N stretching of the quaternary ammonium group in ChCl, while the peak at 1037 cm^{-1} corresponded to C-O stretching of EG [27]. The absorption at 1477 cm^{-1} could be attributed to O-H bending. Notably, compared to the FT-IR spectra of PVA-Gel, NeuroThres-Gel and Ag/PVA-Gel showed negligible shifts in these characteristic peaks, suggesting that the inclusion of Ag NWs or D-Ag NWs would not affect the molecular vibration model in the different microenvironment.

Besides, in the range between 3200 cm^{-1} and 3600 cm^{-1}, a broad absorption band could be observed, attributable to hydrogen-bonded O-H stretching vibrations, which confirmed the presence of an extensive hydrogen-bonded network mainly between the surface hydroxyls of D-Ag NWs and the hydroxyl groups on both PVA chains and EG moieties in the DES. Such a reversible hydrogen-bonded network not only prevented Ag NW aggregation, thereby ensuring uniform dispersion, but also enabled dynamic bond dissociation and reformation in sol-gel transition process, underpinning the gel's thermoplastic recyclability. The X-ray diffraction (XRD) patterns of the samples also revealed distinct features characteristic of PVA (Fig. S1 in Supporting information). A prominent diffraction peak could be observed at $2\theta \sim 19.8°$, corresponding to the (1 0 1) crystalline plane of PVA, indicative of its semicrystalline nature. Additionally, a broad diffraction halo spanning the 2θ range of approximately 15°–25° was evident, which could be attributed to the amorphous regions of PVA.

Benefiting from the densely hydrogen-bonded network, all eutectogels exhibited a freestanding, and gel-like state in ambient conditions (Fig. S2 in Supporting information). Modulus-amplitude oscillatory shearing experiment revealed that the storage modulus (G') of the samples was obviously higher than that of loss modulus (G'') across a broad plateau, confirming the construction of the cross-linked network (Fig. 2C). Notably, NeuroThres-Gel presented the highest plateau modulus of ~47,000 Pa among all the samples, reflecting the enhanced cross-linking density imparted by the hydrogen bonds around the D-Ag NWs. Upon increasing the shearing strain amplitude, a clear crossover point ($G' = G''$) emerged, signifying the onset of network rupture and yielding behavior (Fig. S3 in Supporting information). Meanwhile, PVA-Gel exhibited a transition strain of 21.3 %, which dropped markedly to 8.6 % of Ag/PVA-Gel, likely due to the formation of heterogeneous and rigid Ag NW networks that constrained chain mobility and rendered the structure more brittle. In contrast, the transition strain of NeuroThres-Gel (24.6 %) was similar to that of PVA-Gel (21.3 %), which might be ascribed to the dynamic hydrogen bonding between D-Ag NWs and PVA chains that allows greater network adaptability under strain. These reversible cross-links enabled energy dissipation and structural rearrangement under strain, thereby enhancing the gel's deformation tolerance, elasticity and delaying network rupture. Frequency sweeping measurement further demonstrated excellent frequency independence of the samples over the examined range (Fig. S4 in Supporting information). Both the G' and G'' remained nearly constant across the entire frequency window, with G' consistently exceeding G'' by more than an order of magnitude, indicating a predominantly elastic solid-like response. While PVA-Gel showed a similar frequency-insensitive trend, the markedly higher G' of NeuroThres-Gel suggested a denser and more robust dynamic network formed *via* strong hydrogen bonding between D-Ag NWs and polymer chains.

Notably, incorporation of the DES endowed NeuroThres-Gel with exceptional environmental stability. Long-term aging studies at various storage temperatures further demonstrated the gel's stability: over extended periods, NeuroThres-Gel maintained its weight (Fig. S5A in Supporting information) with negligible decline. Furthermore, the ionic nature of DES contributed to the gel's high conductivity (~0.043 S/m, 30 °C). The presence of mobile ions within the DES facilitated continuous ionic conduction, which remains stable despite environmental fluctuations (Fig. S5B in Supporting information). This remarkable environmental tolerance ensured that the NeuroThres-Gel maintaind its functional performance in practical application, making it a reliable candidate for flexible electronics and wearable sensors.

Benefiting from the dynamic nature of hydrogen bonds, NeuroThres-Gel exhibited intriguing thermoplastic behaviour. Temperature-dependent rheological test revealed a clear sol-gel transition for NeuroThres-Gel (Fig. 2D). Upon heating to 130 °C, G' of NeuroThres-Gel decreased significantly to $\sim 10^2$ Pa, indicating a transition from gel to a sol state with the transition temperature of 109.4 °C. To further evaluate the printability and rheological performance of the inks, shear-dependent viscosity and stress-dependent oscillatory measurements were conducted. As shown in Fig. 2E, both PVA-Gel and Ag/PVA-Gel exhibit a viscosity plateau at low shear rates, indicative of limited molecular mobility and the absence of dynamic interactions within their networks. This resulted in a relatively rigid and less processable gel structure, unfavorable for extrusion-based 3D printing. In contrast, NeuroThres-Gel demonstrated pronounced pseudoplasticity across all tested D-Ag NWs concentrations, characterized by continuous shear-thinning behavior. This rheological advantage stemmed from the thermally responsive dissociation and rearrangement of dynamic hydrogen bonds between D-Ag NWs and PVA chains under shear stress, enabling molecular alignment and reducing flow resistance. Such shear-thinning properties were critical for DIW: High viscosity at rest ensured shape retention after deposition, while low viscosity under shear facilitates easy extrusion without clogging or requiring excessive pressure. Moreover, the zero-shear viscosity of NeuroThres-Gel increased from 7.2×10^4 Pa s to 13.3×10^4 Pa s with increasing D-Ag NWs content (Fig. S6 in Supporting information), further supporting its turnable rheological properties. Collectively, these rheological features confirm the superior 3D printability and dynamic responsiveness of NeuroThres-Gel compared to its counterparts.

As a proof-of-concept demonstration, the NeuroThres-Gel ink could be directly patterned *via* DIW into fully functional, intricately defined sensor architectures with high structural fidelity and uniform filament deposition (Fig. 2F). The printed constructs maintained well-defined edges, showcasing excellent shape retention and print resolution, attributes essential for high-performance soft electronics. In addition, NeuroThres-Gel exhibited exceptional thermoformability and moldability post-curing. Leveraging its in-

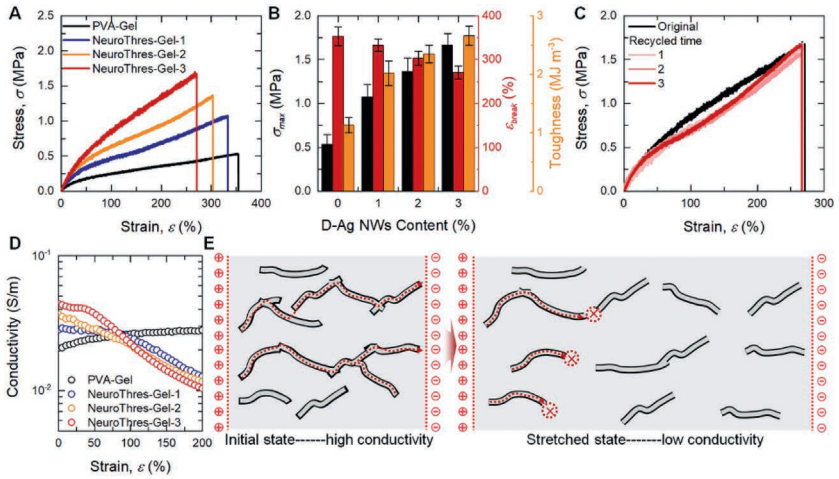


Fig. 3. Mechanoelectrical properties and strain-induced network reconfiguration of NeuroThres-Gel. (A) Tensile stress–strain curves of PVA-Gel, and NeuroThres-Gels. (B) Summary of mechanical properties (tensile strength, elongation at break, and toughness) of NeuroThres-Gels with varying D-Ag NW content. Data are presented as mean ± standard deviation (SD) ($n = 3$). (C) Tensile performance of NeuroThres-Gel-3 over multiple recycling cycles, demonstrating mechanical robustness and reprocessability. (D) *In situ* conductivity of the gels under uniaxial strain, revealing strain-dependent electrical behavior. (E) Schematic representation of dynamic network rearrangement of D-Ag NWs and polymer chains under uniaxial stretching.

herent thermoplasticity, fragmented gel pieces could be remelted and reconfigured into various customized macrostructure shapes (Fig. 2G). These remolded objects preserved fine surface details and complex contours, reflecting the gel's superior processability, surface conformity, and versatility in secondary shaping operations, highlighting its practical potential for sustainable fabrication and iterative prototyping in soft robotic and wearable systems.

The mechanical robustness and structural adaptability of the eutectogels were systematically evaluated to their suitability for e-skin, which need the material with flexible and skin like softness. Uniaxial tensile tests revealed good stretchability of the eutectogels (Fig. 3A). The relationship between filler content and mechanical performance was quantified in Fig. 3B. It could be observed, increasing the D-Ag NW content produced a gradual decrease in elongation at break ($\varepsilon_{\text{break}}$), consistent with a more densely cross-linked network restricting chain mobility. Conversely, maximum tensile strength ($\sigma_{\max}$) and toughness improved with D-Ag NW incorporation, reaching a maximum in the NeuroThres-Gel-3 variant-achieving $\sigma_{\max}$ of 1.68 MPa and toughness of 2.67 MJ/m^3 at comparable strains. Notably, NeuroThres-Gel outperformed its unmodified counterpart (Ag/PVA-Gel) in both strength and toughness (Fig. S7 in Supporting information). To assess the strain hysteresis behavior, loading-unloading tensile tests were performed on the samples. As shown in Fig. S8 (Supporting information), all gels exhibited obvious hysteresis loops, reflecting the viscoelastic nature of the dynamically cross-linked networks. With increasing dynamic cross-linker content, the calculated energy loss coefficient (η) decreased from 0.76 to 0.51, indicating a gradual reduction in energy dissipation and improvement in elastic recovery. In summary, NeuroThres-Gel-3, which exhibited the most comprehensive mechanical performance, is hereafter referred to as NeuroThres-Gel unless otherwise specified. Notably, NeuroThres-Gel demonstrated exceptional mechanical recyclability, after three successive reprocessing cycles (Fig. 3C). This durability was underpinned by its dynamic hydrogen-bonded network, which reversibly dissociated under heat and reforms upon cooling, thereby preserving the gel's structural integrity.

The conductivity of soft materials also played a pivotal role in determining their sensing performance, which was critical for enabling sensing functionalities such as tactile-to-nociceptive signal conversion. Uniaxial tensile tests with *in situ* conductivity measurements (Fig. 3D) revealed that NeuroThres-Gel's electrical conductivity decreases monotonically with increasing strain, and this effect became more pronounced at higher D-Ag NW loadings. In contrast, PVA-Gel, which lacked conductive nanowires, showed low initial conductivity of 0.021 S/m and no strain-dependent conductivity change. Furthermore, the overall conductivity increased with the D-Ag NW content: NeuroThres-Gel-1, NeuroThres-Gel-2, and NeuroThres-Gel-3 reached conductivities of approximately 0.028, 0.035, and 0.043 S/m, respectively.

The above observation indicated that the initial high conductivity of NeuroThres-Gel arises from a well-percolated and dynamically cross-linked network of D-Ag NWs uniformly embedded within the PVA/DES matrix. Upon stretching, the deformation of the polymer chains induced relative displacement between neighboring nanowires, progressively increasing the interparticle spacing and reducing the number of effective conductive junctions. This structural rearrangement disrupted electron-tunneling pathways and weakens the percolation network, resulting in a pronounced decline in conductivity with increasing strain. Such strain-dependent disintegration of the conductive architecture validated the strain-programmed electrical switching behavior observed in Fig. 3E, and further highlights the potential of this material system for programmable tactile-to-pain signal transduction in neuromorphic sensing platforms.

Leveraging its abovementioned intrinsic mechanical flexibility, excellent recyclability, and strain-responsive conductivity, the NeuroThres-Gels exhibited a sensitive and strain-gated mechano-electrical responsive performance. Under uniaxial tensile loading, real-time resistance measurements revealed a two-stage response in $\Delta R/R_0$ (Fig. 4A). In the tactile regime lower than pain threshold strain (ε_t), all NeuroThres-Gels displayed a moderate, linear resistance responsiveness with strain, characterized by low-strain GF_1 values (<3) that rise with D-Ag NW content due to enhanced percolation density. Beyond ε_t, $\Delta R/R_0$ surges nonlinearly, yielding high-strain sensitivity ($GF_2 > 8$), akin to the strain-perception-strengthening effect in biomimetic skins. By contrast, PVA-Gel without Ag NWs maintained a constant low GF value, confirming the necessity of the dynamic nanowire network for threshold switching. Extraction of ε_t from the inflection points in the GF-strain curves demonstrated systematic tunability: increasing D-Ag NW loading from 1 wt% to 3 wt% lowered ε_t from ~100% down to ~80% strain (Fig. 4B). This behavior arises because higher filler concentrations increased junction density, reducing the strain

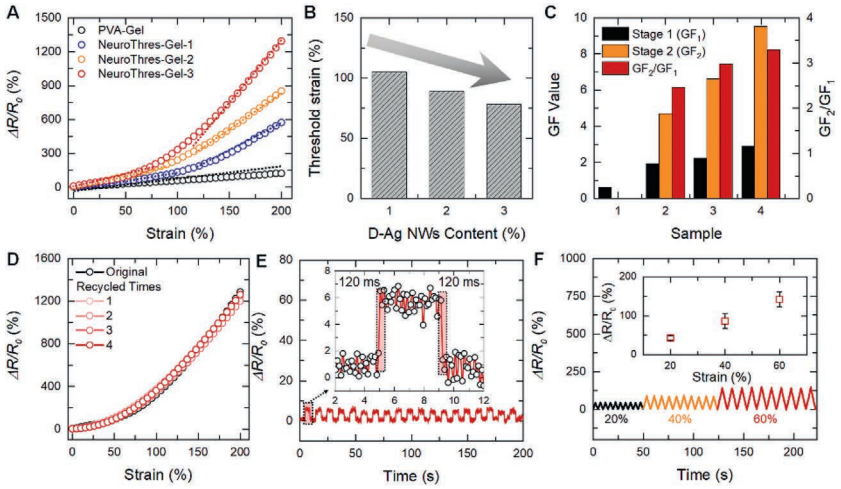


Fig. 4. Mechanoelectrical responsiveness of NeuroThres-Gel. (A) Relative change in resistance of PVA-Gel and NeuroThres-Gels during uniaxial stretching. (B) Threshold strain for activating the mechano-electrical response as a function of D-Ag NW content. (C) GF values of the samples in tactile *vs.* pain-sensing modes and the corresponding GF_2/GF_1 ratios. (D) Relative resistance changes over multiple recycling cycles at 200 % maximum strain. (E) Resistance response patterns during stepwise loading–unloading tests with 0.5 % deformation increments. (F) Resistance variation under cyclic loading at increasing maximum strains (20 %, 40 %, and 60 %).

required to trigger percolation collapse. Correspondingly, the ratio GF_2/GF_1 expanded with nanowire content (Fig. 4C), amplifying the contrast between tactile and nociceptive regimes and enhancing detection fidelity. Importantly, the tunable threshold strain range closely corresponded to the deformation levels associated with nociceptive stimuli in human skin, which typically involved moderate strains, ranging from a few percent to several tens of percent. Moreover, as shown in Fig. S9 (Supporting information), NeuroThres-Gel based sensor maintained stable resistance responses during repeated loading-unloading cycles at 250 % strain, exhibiting intriguing state-independent behavior and excellent mechanical durability.

To confirm the closed-loop functionality, NeuroThres-Gel based sensor were thermally remolded for four successive cycles, with their $\Delta R/R_0$–strain responses remeasured after each cycle (Fig. 4D). The resistance-strain curves of the sensor at different recycling cycles exhibited significant overlap with its original state. These findings underscored the durable and adaptable nature of the e-skin, positioning it as a promising candidate for diverse, dynamic applications requiring high-performance standards.

Dynamic response tests under a small step strain of 0.5 % revealed that the NeuroThres-Gel-based e-skin sensor exhibited a fast electrical signal response and recovery within ~120 ms (Fig. 4E), indicative of its excellent temporal resolution and rapid viscoelastic relaxation behavior. Given that response times of 50–200 ms were widely accepted benchmarks for artificial hydrogel/eutectogel-based sensory systems, this performance was competitive with state-of-the-art platforms and well-suited for real-time detection of transient biomechanical signals. Additionally, the sensor demonstrated a minimum detectable strain of 0.5 %, suggesting a high strain resolution suitable for capturing minute skin deformations. Cyclic tensile tests further revealed the superior mechanical-electrical reliability of the e-skin. As shown in Fig. 4F, the sensor was subjected to repeated loading-unloading cycles at 20 %, 40 %, and 60 % tensile strains. In each case, the electrical resistance signal remained highly consistent across cycles, with well-defined, reproducible peak values. Fig. S10 (Supporting information) highlighted the electrical signal during the period when the applied strain returns to zero, clearly showing the transient recovery and the return of the baseline. To further assess the long-term durability of the sensor, additional cyclic tensile tests were conducted at a strain of 200 % for 1000 consecutive cycles. As shown in Fig. S11 (Supporting information), the electrical resistance signal remained highly stable without noticeable drift or degradation throughout the repeated loading-unloading process, demonstrating the excellent robustness and reliability of the e-skin under large-strain conditions.

To emulate the biologically authentic transition from tactile to nociceptive perception, the design of artificial sensing systems could be guided by the hierarchical structure of the human somatosensory system, in which external stimuli are processed through distinct neural pathways for touch and pain, enabling both signal discrimination and spatial localization (Fig. 5A). In this system, low-intensity mechanical stimuli are transduced by fast-adapting mechanoreceptors and interpreted as tactile signals, while high-intensity or sustained stimuli that exceed a critical threshold activate nociceptors, initiating pain perception and protective responses. Translating this mechanism into synthetic platforms requires materials capable of distinguishing stimulus intensity while also encoding directional and positional information. The NeuroThres-Gel-based sensor implements this biological logic through the abovementioned strain-induced mechanoelectrical responsiveness that enables discrete tactile-to-pain transition and spatially resolved nociceptive feedback.

As a proof-of-concept, the sensor could be affixed to a skeletal knee joint model to monitor mechanical deformation under varying bending angles (Fig. 5B). Although normal knee flexion may not elicit pain in healthy individuals, excessive deformation could induce discomfort in those with joint disorders [37]. At lower bending angles, the sensor maintained a low-resistance state corresponding to tactile-level stimuli. However, at higher angles, the strain on the material exceeded the programmable pain threshold, triggering a sharp increase in resistance (Fig. 5C). The plot of $\Delta R/R_0$ *versus* bending angle clearly showed a nonlinear increase beyond the critical point, enabling real-time pain warning feedback. These results highlight the sensor's potential for early detection and continuous monitoring of joint-related pathologies.

To further demonstrated its capability for biologically inspired tactile–nociceptive sensing, the NeuroThres-Gel-based sensor was affixed onto the surface of a hand model and subjected to increasing uniaxial tensile strain (Fig. 5D). The stretching process was divided into three stages, corresponding to incremental strain levels designed to simulate the transition from gentle deformation to excessive elongation: Stage 1 represented the initial resting

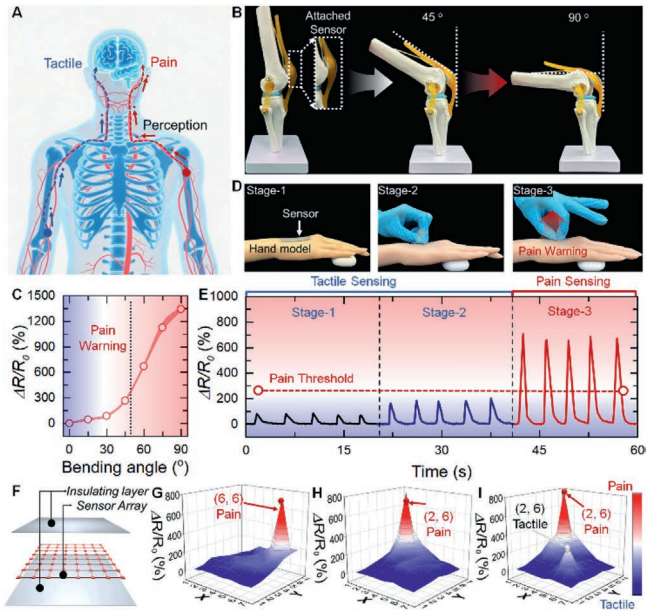


Fig. 5. Tactile-to-pain transition and vectorial mapping capabilities of the NeuroThres-Gel-based sensor. (A) Schematic illustration of the human somatosensory system, highlighting the pathways of tactile and pain perception and the localization of external stimuli. (B) Photographs showing a NeuroThres-Gel sensor attached to a skeletal knee joint model, capturing strain responses under progressive bending angles. (C) $\Delta R/R_0$ of the sensor as a function of bending angle, indicating a distinct threshold between tactile and pain-warning responses. (D) Images of the NeuroThres-Gel sensor applied to a hand model under three increasing levels of mechanical stimulation. (E) Real-time resistance signals recorded during above three stages. (F) Schematic diagram of the pixelated sensor array structure. (G–I) Real-time 3D strain maps recorded from the sensing array.

state without external strain; Stage 2 corresponded to moderate stretching within the tactile-sensing range; and Stage 3 involved high-level stretching that exceeded the critical strain threshold for pain-mode activation. As shown in Fig. 5E, the real-time resistance signal exhibited a distinct transition across the three stages. During Stage 1, the sensor maintained a stable baseline resistance, confirming system stability in the absence of mechanical input. In Stage 2, as the sensor was stretched within the tactile regime, a gradual and reversible increase in resistance was observed, reflecting continuous yet non-damaging mechanical stimulation. Upon entering Stage 3, the applied strain surpassed the programmable threshold, leading to a sharp, non-volatile resistance jump that signified the onset of pain-mode response. This discrete switching behavior effectively mimics the transition from innocuous touch to noxious overstretching, consistent with biological nociceptive mechanisms, offering a promising avenue for intelligent soft robotics and human–machine interfaces.

Leveraging the NeuroThres-Gel's inherent shear-thinning behavior, thermoplasticity, and hierarchical sensing capabilities, we successfully fabricated a pixelated sensor array *via* extrusion-based DIW 3D printing. As illustrated in Fig. 5F, the array was configured in an 8×8 grid layout, with each pixel acting as an independent sensing unit capable of registering localized mechanical strain and executing discrete tactile-to-pain switching. This design emulated the distributed receptive fields of biological skin, allowing the system to identify both the intensity and the precise location of external stimuli. When a substantial mechanical stimulus was applied to designated coordinates such as (6, 6) or (2, 6), the corresponding pixels produced sharply elevated, high-amplitude resistance signals, clearly distinguishing noxious stimuli from benign inputs (Figs. 5G and H). In contrast, when a low-magnitude strain was applied at (6, 2) concurrently with a high strain at (2, 6), the array generated two distinct resistance profiles, enabling simultaneous detection and real-time mapping of both stimulus location and intensity (Fig. 5I). This strain-gated dual-modal sensing behavior empowered the matrix to function as an intelligent interface that not only discriminated tactile *versus* painful stimuli but also achieves precise spatial localization and directional sensing. Such capabilities were essential for advanced neuroinspired prosthetics, robotic skins, and next-generation human-machine interfaces requiring biologically relevant feedback. As summarized in Table S1 (Supporting information), the NeuroThres-Gel sensor achieved an optimized balance of key performance metrics, including broad strain range, rapid response, excellent recyclability, and tunable pain threshold, surpassing most of the reported e-skins.

In summary, we proposed a generalized strain-induced percolation threshold modulation strategy for the development of a recyclable neurothreshold-mimetic eutectogel (NeuroThres-Gel) e-skin capable of strain-programmable tactile-to-pain switching and vectorial nociception. By integrating D-Ag NWs as both dynamic cross-linkers and conductive fillers within a DES-plasticized PVA matrix, the eutectogel exhibited a tunable strain threshold for pain-mode activation (~80 %–100 %), closely mimicking the gating behavior of neuronal action potentials. Below this threshold, the network maintained reversible conductivity for tactile sensing, whereas exceeding it triggered a non-volatile resistance surge due to strain-induced geometric percolation collapse, thereby emulating a nociceptive response. In addition, NeuroThres-Gel displayed excellent shear-thinning behavior, enabling smooth extrusion and high shape fidelity during DIW. Benefiting from the thermoplasticity of the dynamic network, the material could be reshaped and reused multiple times, offering a sustainable and customizable fabrication route. This work established a broadly applicable strategy for engineering neuromorphic e-skins with integrated sensing logic, recyclability, and programmable mechanical responsiveness, opening up promising opportunities in intelligent prosthetics, soft robotics, and human–machine interfaces.

CRediT authorship contribution statement

Xiaohui Yu: Writing – review & editing, Writing – original draft, Visualization, Investigation, Data curation. **Guanpeng Zhou:** Investigation. **Siyan Li:** Investigation. **Yuanfeng Wang:** Investigation. **Juan Zhang:** Investigation. **Xiaotong Fan:** Investigation. **Xiaoshan Fan:** Supervision. **Jiajia Shen:** Supervision, Funding acquisition. **Hui Ma:** Supervision, Funding acquisition. **Zibiao Li:** Writing – review & editing, Supervision.

Declaration of competing interest

The authors declare that they have no known competing financial interests or personal relationships that could have appeared to influence the work reported in this paper.

Acknowledgments

This work is supported by the National Natural Science Foundation of China (No. 52503090), Program of Industrial Development and Research of Jiaxing (No. 2025AC017), Scientific Research Start-up Project of Jiaxing University (Nos. 70525019, 70525028, and 70525013), Agency for Science, Technology and Research (A*STAR) under its RIE2025 Manufacturing, Trade and Connectivity (MTC) Programmatic Funding (No. M22K9b0049).

Supplementary materials

Supplementary material associated with this article can be found, in the online version, at doi:10.1016/j.cclet.2025.112097.

References

[1] R.A. John, N. Tiwari, M.I.B. Patdillah, et al., Nat. Commun. 11 (2020) 4030.
[2] R. Yu, Y. Yan, E. Li, et al., Mater. Horiz. 8 (2021) 2797–2807.
[3] R.S. Dahiya, G. Metta, M. Valle, G. Sandini, IEEE Trans. Robot. 26 (2010) 1–20.
[4] W. Zhou, Y. Yu, P. Xiao, et al., Adv. Mater. 36 (2024) 2403447.
[5] L.E. Osborn, A. Dragomir, J.L. Betthauser, et al., Sci. Robot. 3 (2018) eaat3818.
[6] X. Yu, Y. Wang, H. Zhang, et al., Chem. Mater. 35 (2023) 9287–9298.
[7] X. Yu, Z. Wang, Z. Li, X. Fan, T. Liu, Chem. Mater. 36 (2024) 9822–9833.
[8] P. Xiao, W. Zhou, Y. Liang, et al., Adv. Funct. Mater. 32 (2022) 2201812.
[9] F. Li, S. Gao, Y. Lu, et al., Adv. Sci. 8 (2021) 2004208.
[10] F. Sun, J. Xu, T. Liu, et al., Mater. Horiz. 8 (2021) 3356–3367.
[11] J.S. Hong, J.H. Lee, Y.W. Nam, Carbon 61 (2013) 577–584.
[12] Y. Huang, X. Zhang, T. Zhu, et al., Chem. Mater. 35 (2023) 5809–5821.
[13] S. Li, H. Yang, N. Zhu, et al., Adv. Funct. Mater. 33 (2023) 2211189.
[14] M. Cadena, L. Ning, A. King, et al., Adv. Healthc. Mater. 10 (2021) 2001600.
[15] L. Wertheim, R. Edri, Y. Goldshmit, et al., Adv. Sci. 9 (2022) 2105694.
[16] H. Wei, M. Lei, P. Zhang, et al., Nat. Commun. 12 (2021) 2082.
[17] X. Xu, Y. Lyu, D. Liu, et al., Small 21 (2025) 2411808.
[18] J. Zheng, G. Chen, H. Yang, et al., Mater. Horiz. 10 (2023) 4232–4242.
[19] M. Ho, A.B. Ramirez, N. Akbarnia, et al., Adv. Funct. Mater. 35 (2025) 2415507.
[20] J. Liu, J. Garcia, L.M. Leahy, et al., Adv. Funct. Mater. 33 (2023) 2214196.
[21] Q. Wu, Y. Xu, S. Han, et al., ACS Nano 18 (2024) 31148–31159.
[22] F. Puza, K. Lienkamp, Adv. Funct. Mater. 32 (2022) 2205345.
[23] P. Wang, Q. Liao, B. Yuan, H. Zhang, ACS Appl. Mater. Interfaces 15 (2023) 32945–32956.
[24] S. Ullah, J. Shen, H.T. Xu, Chin. Chem. Lett. 36 (2025) 110553.
[25] T. Xu, K. Chen, Z. He, et al., Chin. Chem. Lett. 37 (2026) 111959.
[26] C. Yu, H. Lin, L. Li, et al., Chin. Chem. Lett. 37 (2026) 111946.
[27] X. Yu, C.P. Teng, J.C.C. Yeo, et al., Adv. Funct. Mater. 35 (2025) 2501677.
[28] X. Yu, Y. Zheng, H. Zhang, et al., Chem. Mater. 33 (2021) 6146–6157.
[29] X. Pan, H. Gao, Y. Su, et al., Nano Res. 11 (2018) 410–419.
[30] Y. Zhang, X. Yu, Y. Wang, et al., ACS Appl. Mater. Interfaces 17 (2025) 4165–4175.
[31] H. Wu, Z. Pang, L. Ji, et al., Chem. Eng. J. 497 (2024) 154883.
[32] S. Du, X. Chen, M. Li, et al., Adv. Funct. Mater. 35 (2025) 2409726.
[33] S. Hu, J. Song, Q. Tian, et al., Adv. Fiber. Mater. 6 (2024) 1980–1991.
[34] Y. Shao, C. Dang, H. Qi, et al., Matter 7 (2024) 4076–4098.
[35] J. Li, C. Wang, Y. Xing, et al., ACS Sustain. Chem. Eng. 11 (2023) 10578–10589.
[36] J.R. Olles, P. Slavik, N.K. Whitelaw, D.K. Smith, Angew. Chem. Int. Ed. 58 (2019) 4173–4178.
[37] V. Duong, W.M. Oo, C. Ding, A.G. Culvenor, D.J. Hunter, JAMA 330 (2023) 1568–1580.